JACS
JOURNAL OF THE AMERICAN CHEMICAL SOCIETY
Article
Cite This: J. Am. Chem. Soc. 2019, 141, 6680−6689
pubs.acs.org/JACS

Lithium-Doping Stabilized High-Performance P2−$Na_{0.66}Li_{0.18}Fe_{0.12}Mn_{0.7}O_2$ Cathode for Sodium Ion Batteries

Lufeng Yang,[†] Xiang Li,[‡] Jue Liu,[§] Shan Xiong,[†] Xuetian Ma,[†] Pan Liu,[∥] Jianming Bai,[⊥] Wenqian Xu,[#] Yuanzhi Tang,[∥] Yan-Yan Hu,[‡,▽] Meilin Liu,[⊗] and Hailong Chen*[,†]

[†]The Woodruff School of Mechanical Engineering, Georgia Institute of Technology, 771 Ferst Drive, Atlanta, Georgia 30332-0245, United States
[‡]Department of Chemistry and Biochemistry, Florida State University, Tallahassee, Florida 32306, United States
[§]Neutron Scattering Division, Oak Ridge National Laboratory Oak Ridge, Tennessee 37830, United States
[∥]School of Earth and Atmospheric Sciences, Georgia Institute of Technology, 311 Ferst Drive, Atlanta, Georgia 30332-0340, United States
[⊥]National Synchrotron Light Source II, Brookhaven National Laboratory, Upton, New York 11973, United States
[#]Argonne National Laboratory, 9700 South Cass Avenue, Building 433-D003, Argonne, Illinois 60439, United States
[▽]National High Magnetic Field Laboratory, 1800 East Paul Dirac Drive, Tallahassee, Florida 32310, United States
[⊗]School of Materials Science and Engineering, Georgia Institute of Technology, 771 Ferst Drive, Atlanta, Georgia 30332-0245, United States

Supporting Information

ABSTRACT: While sodium-ion batteries (SIBs) hold great promise for large-scale electric energy storage and low speed electric vehicles, the poor capacity retention of the cathode is one of the bottlenecks in the development of SIBs. Following a strategy of using lithium doping in the transition-metal layer to stabilize the desodiated structure, we have designed and successfully synthesized a novel layered oxide cathode P2−$Na_{0.66}Li_{0.18}Fe_{0.12}Mn_{0.7}O_2$, which demonstrated a high capacity of 190 mAh g^{-1} and a remarkably high capacity retention of ∼87% after 80 cycles within a wide voltage range of 1.5−4.5 V. The outstanding stability is attributed to the reversible migration of lithium during cycling and the elimination of the detrimental P2−O2 phase transition, revealed by ex situ and in situ X-ray diffraction and solid-state nuclear magnetic resonance spectroscopy.

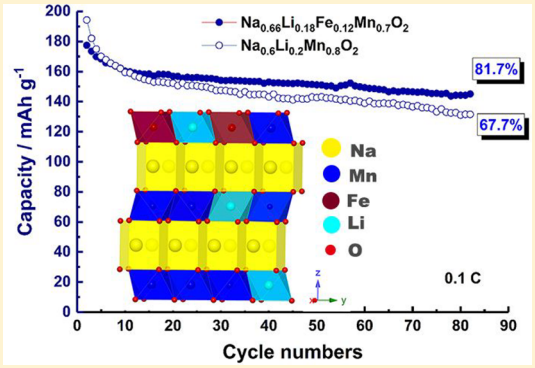

1. INTRODUCTION

Recently, sodium ion batteries (SIBs) have been attracting ever increasing attention for their great potential in applications in electrical grid energy storage and low speed electric vehicles. The specific energy density of cathode is one of the key performance-limiting factors for SIBs. Among different cathode materials, layered sodium transition-metal oxides (Na_xMO_2) were extensively studied because of their high theoretical specific capacity (∼220−270 mAh g^{-1})[1,2] as well as the use of low-cost, earth-abundant, and low-toxicity transition metals such as Fe and Mn. While most lithium layered oxides adopt an O3 structure (following Delmas's notation[3]), sodium layered oxides have more thermodynamic stable structures, such as O3, P3, and P2, different in the concentration and crystallographic site of Na^+ ions, and the stacking sequence of the anions. Previous reports showed that many P2 and O3 cathodes can deliver reasonably high capacities of about 40−60% of the theoretical value (e.g., ∼120−150 mAh g^{-1}) and good cycling stability within the voltage window of ∼1.5−4.1 V, corresponding to a moderate depth of cycling.[4] However, attempts to obtain higher capacity (deeper cycling) were hindered, mainly due to undesirable irreversible phase transition taking place at the deeply charged states. The P2-structured cathode undergoes a P2′ → P2 → (sometimes through OP4) → O2 type phase evolution pathway.[2,5] The complex multiple two-phase reactions are detrimental to the cycling because these phase transitions, such as the P2−O2 transition, are degenerate.

During charging, the original P2 structure can transform to the O2 phase with, in theory, two possible directions of gliding the oxygen layer, as shown in Figure 1, thus being 2-fold degenerate. Practically, within one particle (a small single crystal), because Na extraction can take place simultaneously at different regions on the exposing facets, the gliding of oxygen layer likely is not concerted throughout the whole crystal.

Received: February 17, 2019
Published: April 1, 2019

DOI: 10.1021/jacs.9b01855
J. Am. Chem. Soc. 2019, 141, 6680−6689

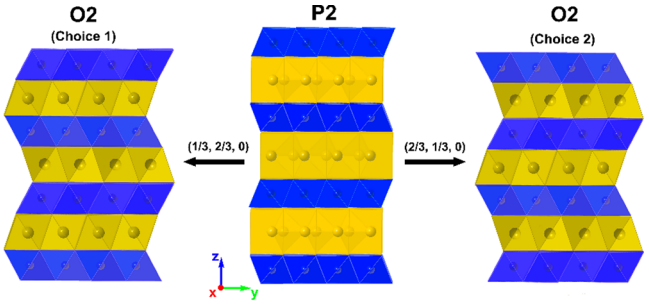

Figure 1. Schematic illustrations of P2 type and two choices of O2 type structures.

Lattice mismatch and dislocations then form, not only at the domain boundaries between the deeply desodiated domain (O2 or OP4) and the shallowly desodiatied domain (P2) but also at the boundaries between O2 domains with different gliding directions. The formation of such dislocations is partially but not fully reversible. The accumulation of such dislocations over extended cycling can crash the particle or produce stairlike deformation and eventually degrade the cathode, as suggested by the computational investigation by Van der Ven et al.[6,7] For this reason, most previous works have limited the operation window to 2.0−4.0 V to avoid the P2−O2 transition and thus improve its cycle life, yet at the price of significantly lowering the available capacity and energy density.[8−10]

Strategies have been trialed to delay or eliminate the P2−O2 transition such as doping with a wide variety of cations in the transition metal (TM) sites.[11−19] In our previous work,[12] we have demonstrated that doping lithium into the manganese site is a promising strategy because the clustering between the high-valent cation (Mn^{4+}) and the low-valent Li^+ can effectively pin the adjacent oxygen layer and make the P2−O2 gliding difficult. Doping of lithium was also previously demonstrated to be effective in the works by Kim et al. on P2−$Na_{0.85}Li_{0.17}Ni_{0.21}Mn_{0.64}O_2$,[14] Meng et al. on P2−$Na_{0.80}[Li_{0.12}Ni_{0.22}Mn_{0.66}]O_2$,[15] Clément et al. on $Na_x[Li_yNi_zMn_{1-y-z}]O_2$,[20] and Bianchini et al. on P2−O3 $Na_{2/3}Li_{0.18}Mn_{0.8}Fe_{0.2}O_2$[21] cathodes, yet the capacity of these compounds were still below 150 mAh g^{-1}. In our previous work, $Na_{0.6}Li_{0.2}Mn_{0.8}O_2$ exhibited a very high initial capacity of 223 mAh g^{-1} within a 1.5−4.5 V window with a reasonably good capacity retention.[12] One of the reasons for the capacity decay is the loss of lithium during cycling. Keeping the Li dopant in the transition metal layer upon long term cycling is key to stabilize the layered structure. In this work, we designed a new P2 compound P2−$Na_{0.66}Li_{0.18}Fe_{0.12}Mn_{0.7}O_2$, with co-doped Li and Fe in the TM layer with the rationale that higher redox voltage caused by the Fe^{3+}/Fe^{4+} may help keep Li in the lattice during cycling. The synthesis, electrochemical testing, and characterizations are elaborated below.

2. EXPERIMENTAL SECTION

Material Preparation. The P2−$Na_{0.66}Li_{0.18}Fe_{0.12}Mn_{0.7}O_2$ compounds were synthesized by solid-state reaction from starting materials of sodium carbonate (Na_2CO_3, Alfa Aesar, 99.7%), lithium carbonate (Li_2CO_3, Alfa Aesar, 99.7%), iron oxide (Fe_2O_3, Alfa Aesar, 99.8%), and manganese oxide (MnO_2, Alfa Aesar, 99.7%) with stoichiometric ratios. Both lithium and sodium sources were used in 5% excess to compensate for their loss during calcination. The starting materials were mixed in a stoichiometric ratio and ground via a planetary high-energy ball mill (Retsch PM200) at 300 rpm for 2 h. The mixture was then pressed into pellets and calcined in air at 850 °C for 12 h with a ramping rate of 5 °C per minute. After heating, the pellets were quenched to room temperature by quickly placing them on a copper plate. The quenched pellets were then transferred to an Ar-filled glovebox immediately to minimize contact with air and moisture.

Electrochemical Testing. P2−$Na_{0.66}Li_{0.18}Fe_{0.12}Mn_{0.7}O_2$ active material (85 wt %) and carbon black (15 wt %, Super P, Timcal) were first mixed in a Retsch PM200 planetary ball mill at 300 rpm for 2 h to achieve a homogeneous mixture and a carbon coating on the surface of the active material particle. Positive electrodes were then prepared by mixing the carbon coated active material (80 wt %) with additional carbon black (10 wt %, Super C65, TIMCAL) and polivinylidene difluoride (PVdF, 10 wt %, 6020 Solef, Arkema Group). The slurry was made by adding an appropriate amount of *N*-methyl-2-pyrrolidone (NMP). After thorough hand mixing, the slurry was cast onto an aluminum foil and dried at 100 °C in a vacuum oven overnight. The dried film was roll-pressed and cut into round disks of 15 mm diameter. Sodium metal foil was used as the negative electrodes. The electrolyte solution was $NaPF_6$ (1 molar) dissolved in propylene carbonate (PC). A piece of glass fiber filter GF/D (Whatman) was used as the separator. CR2016-type coin cells were then assembled in an Ar-filled glovebox and tested with an Arbin battery cycler (BT2043).

Material Characterization. X-ray diffraction (XRD) patterns were first collected using a Bruker D8 Advance diffractometer equipped with a molybdenum source. The crystalline structure of the sample was further investigated using synchrotron radiation source (λ = 0.2362 Å) at Beamline 28-ID-2 at the National Synchrotron Light Source II (NSLS-II) at Brookhaven National Laboratory , Upton, NY. Selected samples were also tested using synchrotron radiation source (λ = 0.3943 Å) at Beamline 17-BM at the Advanced Photon Source (APS) at the Argonne National Laboratory (ANL), Lemont, IL. *Operando* XRD of the samples were first performed on the Bruker D8 with an in situ battery cell in reflection mode. The in situ cell was charged/discharged within a voltage domain of 1.5−4.5 V at a rate of C/20. *Operando* synchrotron XRD (SXRD) on selected samples were also performed using synchrotron radiation source at Beamline 28-ID-2 at NSLS-II using an in situ battery cell in transmission mode, and XRD patterns were collected every 5 min. The in situ cell used for lab X-ray consists of single-sided beryllium window, as used in previous work.[22] The in situ cell used for synchrotron X-ray consists of two-sided windows, as used in previous work.[23] Morphological investigation of the samples was conducted using field-emission scanning electron microscopy (FE-SEM, Hitachi SU8010). Mn and Fe K-edge X-ray adsorption near edge structure (XANES) spectroscopy analyses were conducted at Beamlines 5-BM-D of APS using Si (111) monochromators and with 40% detuning to avoid higher order harmonics. XANES data were collected from −50 to 200 eV in both transmission and fluorescence modes using a vortex detector. Neutron diffraction (ND) data were collected at the NOMAD beamline at the Spallation Neutron Source (SNS) at Oak Ridge National Laboratory (ORNL).[24] Two 30 min scans were collected and averaged to improve the signal-noise ratio. The obtained diffraction data were normalized against a vanadium rod and background subtracted. The conversion from time-of-flight to *d*-spacing was done using second order polynomial parameters (TOF = d_0 + *dfc*·d + *dfa*·d^2) calibrated from a NIST Si 640d standard sample. During the refinement, d_0 and *dfc* were fixed to the values refined from Si standard while *dfa* was allowed to vary to account for the sample displacement and absorption induced diffraction peak shifts. The diffraction peak shapes were primarily modeled using a pseudo-Voigt function, with an additional convolution of exponential function to model the asymmetrical diffraction peaks. Fundamental parameters approach[25] was used for the Rietveld refinement of synchrotron XRD data. ^{7}Li magic-angle spinning (MAS) NMR experiments were performed on a Bruker Avance III spectrometer in a 14.1 T magnetic field with a ^{7}Li Larmor frequency of 194.34 MHz. Electrodes were packed into 2.5 mm rotors and spun at a MAS rate of 25 kHz. The pjMATPASS pulse sequence was employed to achieve high-resolution NMR spectra. The

DOI: 10.1021/jacs.9b01855
J. Am. Chem. Soc. 2019, 141, 6680−6689

recycle delay was 0.3 s, and the 90° pulse length was 1.0 μs. LiCl(s) with a ^{7}Li chemical shift at 0 ppm was used as a reference.

3. RESULTS

3.1. Synthesis and Structure Characterization. A group of Li and Fe co-doped Mn-based layered compounds with general formula $Na_xLi_yFe_zMn_{(1-y-z)}O_2$, with z ranging from 0.4 to 0.12, were synthesized by a solid state method. The XRD patterns of the materials (Figure S1) reveal that P2 phase is more favored for Fe-poor compositions, whereas O3 phase is more favored for Fe-rich compositions. A phase pure P2 compound, $Na_{0.66}Li_{0.18}Fe_{0.12}Mn_{0.7}O_2$, was successfully synthesized with the Fe content being lowered to 0.12 per formula unit. The long-range structure of the sample was characterized by high-resolution synchrotron X-ray diffraction (SXRD) and neutron diffraction (ND). The SXRD pattern in Figure 2a shows a single phase with Bragg peaks expected for a typical P2 phase with hexagonal space group $P6_3/mmc$. Rietveld refinement was conducted using this space group and by placing Mn, Fe, Li ions in octahedral sites of the transition-metal layer and Na ions at the two trigonal prismatic sites in the alkaline metal layer. The Na site sharing face with adjacent oxide layers is denoted as Na_f and the edge-sharing site is denoted as Na_e. The refinement shows excellent goodness of fit with this model. The occupancy of the Na_e and Na_f sodium sites were refined to be 0.395(5) and 0.251(4), respectively, showing a preferred occupancy at Na_e site, which was also observed in other P2 compounds.[8] The low intensity diffraction peaks at 4.02 and 4.76 Å shown in Figure 2a cannot be refined with this model structure. The peak at 4.02 Å can be assigned to the "1/3 1/3 0" superlattice, a commonly seen Li^+/Mn^{4+} in plane ordering with a $\sqrt{3}a \times \sqrt{3}a$ -type supercell in Li_2MnO_3 and Li-excess cathode materials,[26,27] while the peak at 4.76 Å can be assigned to trace amount impurities.

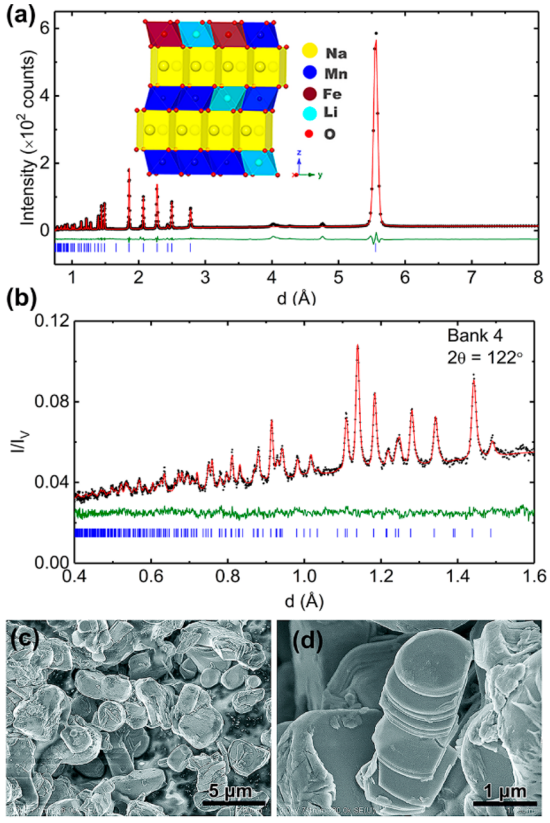

Figure 2. Synchrotron XRD (a) and neutron diffraction (b) patterns and Rietveld refinement of the pristine P2–$Na_{0.66}Li_{0.18}Fe_{0.12}Mn_{0.7}O_2$ powder : (black dots) experiment data; (red line) calculated data; (green line) residue; (blue vertical bar) Bragg peak positions. Inset in (a) shows the crystal structural of a refined P2-type layered oxide. (c) and (d) are SEM images of the as-prepared pristine sample at different magnifications.

ND data was further analyzed to investigate whether cation ordering exists in the TM layers. No characteristic peaks of Mn/Fe ordering in the TM layers were observed (Figure 2b), indicating no long-range ordering between Mn and Fe. On the other hand, the ordering of Li–Mn/Fe is expected given the large difference in their charge and ionic radii, but it is expected to be critically important to hinder the gliding of the oxygen layer in the pending P2–O2 phase transitions.[12] The refined cell parameters and atomic positions based on SXRD and ND are present in Tables 1 and 2, respectively, which are in good agreement with each other and with low R_{wp} values, further confirming the proposed structural model. As shown in Figure 2c,d, the as-prepared particles have a hexagonal cylindrical morphology with an average size of 2–5 μm, in agreement with the hexagonal symmetry of the lattice.

Table 1. Rietveld Refinement Results on the SXRD Pattern of $Na_{0.66}Li_{0.18}Fe_{0.12}Mn_{0.7}O_2$ [a–c]

atom	site	x	y	z	occ	B_{iso}
Na_e	2d	0.3333	0.6667	0.75	0.395(5)	2.8(2)
Na_f	2b	0	0	0.25	0.251(4)	2.8(2)
Li	2a	0	0	0	0.185(7)	1
Fe	2a	0	0	0	0.115(7)	0.22(2)
Mn	2a	0	0	0	0.7	0.22(2)
O	4f	0.3333	0.6667	0.0919(3)	1	0.83(10)

[a]Space group $P6_3/mmc$ (No. 194). [b]$a = b = 2.88293$ (19) Å, $c = 11.1155$ (7) Å, $V = 80.007(12)$ Å^3. [c]$R_{wp} = 7.45\%$.

Table 2. Rietveld Refinement Results on the ND Pattern of $Na_{0.66}Li_{0.18}Fe_{0.12}Mn_{0.7}O_2$ [a–c]

atom	site	x	y	z	occ	B_{iso}
Na_e	2d	0.3333	0.6667	0.75	0.379(7)	3
Na_f	2b	0	0	0.25	0.265(6)	3
Li	2a	0	0	0	0.184(3)	2
Fe	2a	0	0	0	0.116(3)	1.4(5)
Mn	2a	0	0	0	0.7	0.48(1)
O	4f	0.3333	0.6667	0.0915(9)	1	0.74(3)

[a]Space group $P6_3/mmc$ (No. 194). [b]$a = b = 2.8768(4)$ Å, $c = 11.1154(15)$ Å, $V = 79.67(2)$ Å^3. [c]$R_{wp} = 2.74\%$, $\chi^2 = 1.06$.

3.2. Electrochemical Characterization. P2–$Na_{0.66}Li_{0.18}Fe_{0.12}Mn_{0.7}O_2$ was cycled as the cathode in half cells. Representative galvanostatic charge/discharge profiles upon cycling are shown in Figure 3a. The electrode exhibited an initial charge and discharge capacity of 343 and 214 mAh g^{-1} at 10 mA g^{-1} within 1.5–4.5 V, respectively. The very high initial charge capacity apparently cannot be solely attributed to transition-metal redox reactions. As also reported for other Li-rich Mn based layered oxides cycled at high voltage (>4.2 V), the contribution in capacity from the decomposition of electrolyte and oxygen evolution (including O_2 release and lattice oxygen redox) is expected.[28–30] This part of the capacity features in two voltage slopes centered at around 4.0 and 4.4 V,

DOI: 10.1021/jacs.9b01855
J. Am. Chem. Soc. 2019, 141, 6680–6689

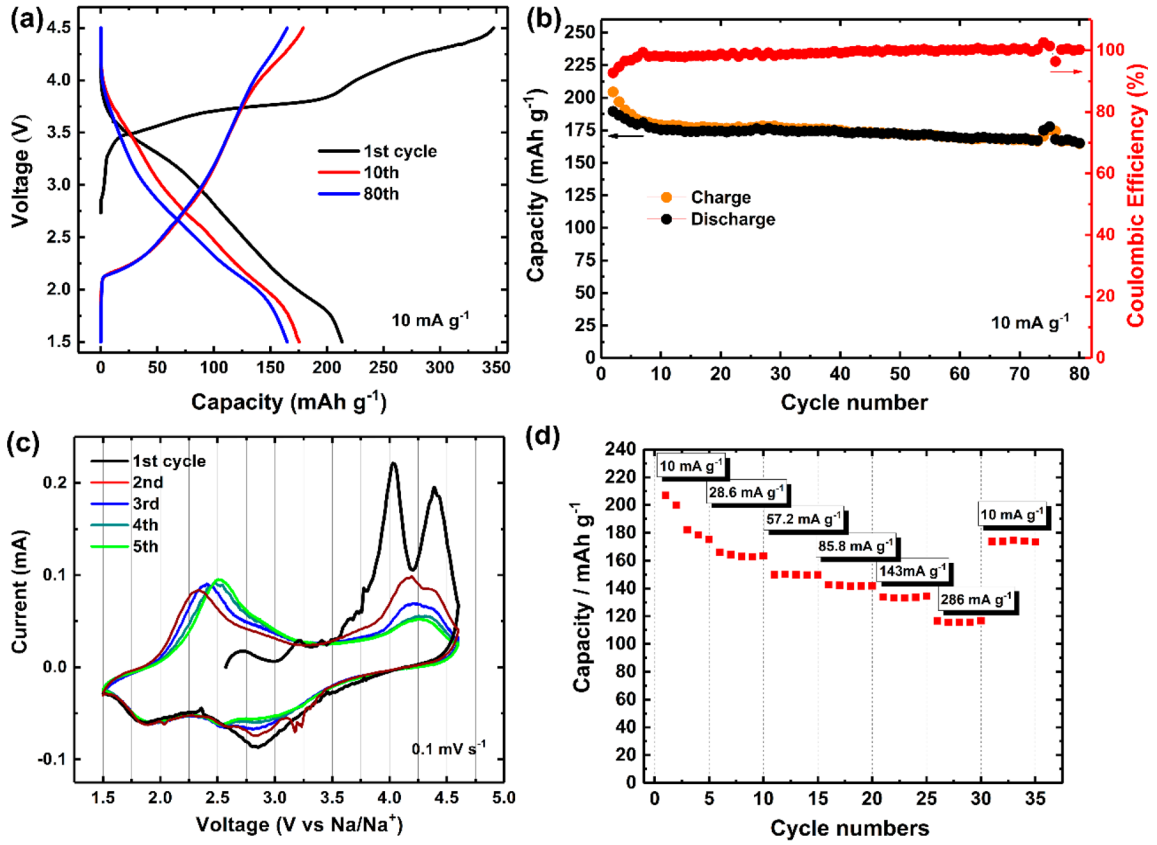

Figure 3. Electrochemical characterization of $Na_{0.66}Li_{0.18}Fe_{0.12}Mn_{0.7}O_2$ in Na haft-cells: (a) representative charge/discharge curves at 10 mA g^{-1} in the voltage range of 1.5−4.5 V, (b) charge/discharge capacity and Coulombic efficiency as a function of cycle number, (c) cyclic voltammogram curves collected within a voltage range of 1.5−4.6 V, and (d) rate capability.

respectively. This can be more clearly seen in the cyclic voltammetry (CV) curve of the first cycle in Figure 3c. The two cathodic peaks quickly drop in consequent cycles, indicating that for the most part these two processes are irreversible, which is speculated to be associated with O_2 gas release and passivation of the surface of the cathode particles. These irreversible processes are similar to the previously reported results of lithium-rich layered oxides,[30−34] considering the 0.3 V difference in electrode potential of Na/Na^+ vs Li/Li^+. With that said, the initial discharge capacity of 214 mAh g^{-1}, which does not include electrolyte decomposition that only takes place in charging, is very high among reported layered oxide cathodes. Although a slight decrease in discharge capacities was witnessed in the first 10 cycles, the electrode exhibited a very stable cycling performance in the following cycling, as shown in Figure 3b. The discharge capacity of the second cycle was 190 mAh g^{-1} and remained ∼165 mAh g^{-1} after 80 cycles, indicating an excellent capacity retention of 86.8% in 80 cycles and an average capacity retention of 99.82% per cycle.

The voltage profiles in the second and following cycles are slopping (Figure S2), and no obvious plateaus were identified, indicating a predominant solid solution type phase evolution pathway, which is different from those previously reported for the Li-free P2-type $Na_xFe_yMn_{1-y}O_2$ ($0 \le y \le 0.5$) cathodes.[8−10] The Li-free P2 cathodes show several voltage steps in their electrochemical profiles, indicating one or more two-phase reactions during cycling and subsequently leading to limited cyclability. Figure 3c shows the CV curves of the $Na_{0.66}Li_{0.18}Fe_{0.12}Mn_{0.7}O_2$ electrode within a voltage range of 1.5−4.6 V at a scan rate of 0.1 mV s^{-1}. The main feature of the Mn^{3+}/Mn^{4+} redox process is reflected by a pair of anodic/cathodic peaks in the CV curves at the voltage region of 2−3 V. The two pronounced anodic peaks associated with electrolyte decomposition and oxygen activities in the first CV curve shifted toward each other and merged into one broad peak centered at ∼4.27 V in the following cycles, indicating the stabilization of the structure and the surface after plausible structure rearrangement and surface passivation. The rate capability of the $Na_{0.66}Li_{0.18}Fe_{0.12}Mn_{0.7}O_2$ electrode was investigated in a slow-charge−fast-discharge mode (Figure 3d) by measuring cells at discharge current densities of 10, 28.6, 57.2, 85.8, 143, and 286 mA g^{-1} while maintaining the charging current constant at 10 mA g^{-1}. As a result, the sample displays good rate capability, retaining 93.7% capacity at C/10, 86.2% at C/5, 81.6% at C/3, 77% at C/2, and 66% at 1 C, repectively, compared to the capacity under 10 mA g^{-1} rate (the last cycle value over 5 cycles at each rate). After the rate test, the cell was again cycled at 10 mA g^{-1} rate and still demonstrated a capacity of ∼180 mAh g^{-1}.

To evaluate the effect of Li doping on the performance of $Na_{0.66}Li_{0.18}Fe_{0.12}Mn_{0.7}O_2$ electrode, the electrochemical data of Li-free material $Na_xFe_yMn_{1-y}O_2$ in literature was compared. Table S1 shows the comparison of electrochemical performance between Li-free P2-type $Na_xFe_yMn_{1-y}O_2$ ($0 \le y \le 0.5$) cathodes and the $Na_{0.66}Li_{0.18}Fe_{0.12}Mn_{0.7}O_2$ material in this study. Within the given wide voltage range from 1.5−4.5 V, the electrochemical performance of the electrodes in this study outperform almost all of the previously reported Li-free $Na_xFe_yMn_{1-y}O_2$ electrodes,[8,10,13,35−37] which were cycled

DOI: 10.1021/jacs.9b01855
J. Am. Chem. Soc. 2019, 141, 6680−6689

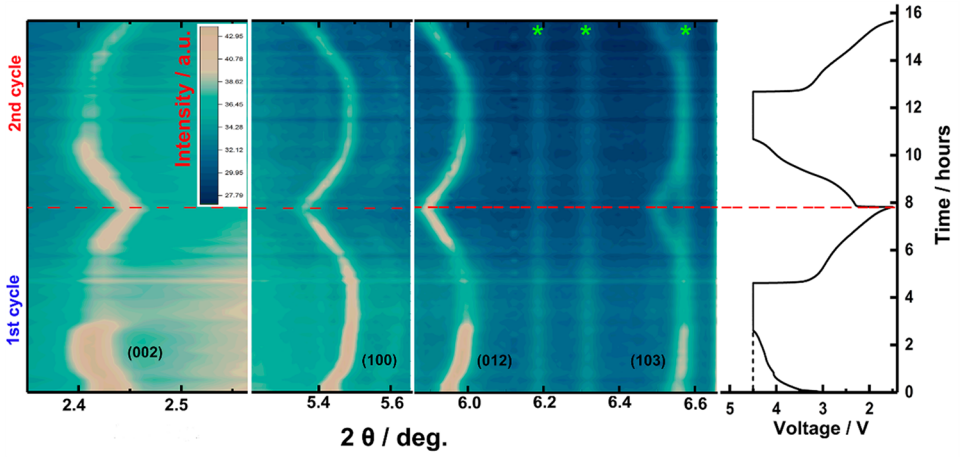

Figure 4. Representative 2θ regions of *operando* synchrotron XRD data highlighting the evolution of the (002), (100), (012), and (103) reflections in $Na_{0.66}Li_{0.18}Fe_{0.12}Mn_{0.7}O_2$, shown in both contour maps (left) and charge/discharge profiles (right). The constant diffraction intensity in the regions marked with * represent the diffraction contribution from in situ cell background such as the beryllium window and the current collector Al.

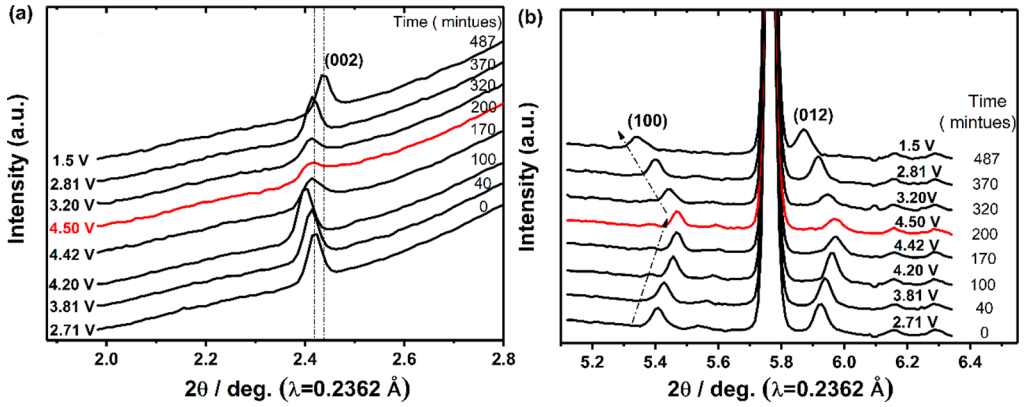

Figure 5. Snapshots of *operando* synchrotron XRD patterns of (a) (002) and (b) (100) and (012) reflections. The strong static reflection at ~5.76° is from the Be window.

within a smaller voltage window to avoid potential irreversible phase transition.

3.3. Characterization of Structural Evolution. The structural evolution of $Na_xLi_{0.18}Fe_{0.12}Mn_{0.7}O_2$ induced by the intercalation and deintercalation of sodium ions was first examined by *operando* laboratory X-ray diffraction (Figure S3) at a cycling rate of C/20. The results indicate a solid solution type phase evolution within a wide voltage range of 1.5−4.5 V, with no new phase observed other than the shift of the peak position and change of peak intensity for the original P2 phase. Representative fitting results of the diffraction patterns collected at high or low voltage values are shown in Figure S4. No additional peaks corresponding to the O2 or OP4 phase are seen even at 4.5 V, and no distinct split of the (00*l*) peaks is noticed upon discharge to 1.5 V, further confirming the absence of the P2′ phase in this material at low potential, which commonly appear in Na_xMnO_2 or $Na_xFe_yMn_{1-y}O_2$ materials during cycling.[8−10,37,38]

High-resolution *operando* synchrotron X-ray diffraction was also employed to further explore the structural evolution during cycling. Again, no new phases were observed with high-resolution SXRD. Figure 4 shows the contour map of the SXRD patterns in the first two cycles. The changes in the peak position and intensity with time are obvious for the (002), (100), (012), and (103) reflections, further confirming a single-phase pathway. Selected SXRD patterns in the first (or second) cycle are shown in Figure 5. During charge with the sodium deintercalation, the (002) reflection first moved to lower angle then to higher angle, indicating an expansion followed by a contraction along the *c*-axis. Such phenomenon can be attributed to the slight slipping of the transition metal (MO_2) layers to alleviate the increasing electrostatic repulsion between them, leading to the formation of a "minor P2" phase with smaller *c* lattice.[26] Meanwhile, the (100) and (012) reflections constantly moved to higher angle, suggesting a contraction in the *ab* plane. In addition, an obvious loss of intensity and considerable line broadening was witnessed at high voltage range for the (002) reflection, indicating a decrease in long-range ordering, presumably caused by the deviations from the ideal P2 stacking sequence. Upon discharge, all of the origin reflections recovered without new reflections observed, indicating a very reversible structural transformation during cycling. This rather reversible phase evolution shows that Li-substitution indeed improves the stability of the Mn based P2 phase within a wide voltage window, which accounts for the excellent cycling stability of $Na_{0.66}Li_{0.18}Fe_{0.12}Mn_{0.7}O_2$. Of course, many factors could cause capacity fade, besides the irreversible phase transitions, such as

DOI: 10.1021/jacs.9b01855
J. Am. Chem. Soc. 2019, 141, 6680−6689

the cyclic strain and stress change and the migration of the transition metal. But the elimination of the irreversible P2−O2 transition drastically improved the reversible capacity, presenting a significant improvement.

Analysis of the laboratory in situ XRD patterns (Figure S3) was conducted to gain more understanding of the structural evolution of the electrode materials upon sodium intercalation/deintercalation. Figure S5 shows the evolution of the sodium occupancy in the electrode materials and their lattice parameter upon the first charge/discharge process. The reversible evolution of *a* and *c* lattice parameters of the P2−$Na_{0.66}Li_{0.18}Fe_{0.12}Mn_{0.7}O_2$ electrode during the charge and discharge indicates a high stability of the P2 structure and excellent reversibility upon Na insertion/extraction. Notably, the largest percentage of volume change upon charge and discharge was calculated to be only 3.5%. Such a low cell volume change revealed that the origin P2 phase likely did not transform into O2 phase or OP4 phase, which was previously reported to be involved in large volume changes of 30% and 13%, respectively.[26]

In addition, structural stability of P2−$Na_{0.66}Li_{0.18}Fe_{0.12}Mn_{0.7}O_2$ upon long-term cycling was further examined by SXRD. The cycled sample was obtained from a coin cell after 100 cycles. Figure 6 shows that the XRD patterns of the pristine and cycled samples are almost identical. The refection at around 3.4° 2θ corresponding to the superstructure of Li/Mn is still seen. The X-ray reflections at around 2.8 and 6.7° were also observed, which can be assigned to impurity that disappeared after long-term cycling, along with the intensity of (112) reflection becoming more pronounced when compared with the adjacent reflections. Nevertheless, no reflections corresponding to other new phase was found for the long-term cycled electrode sample, demonstrating its high structural stability upon prolonged cycling.

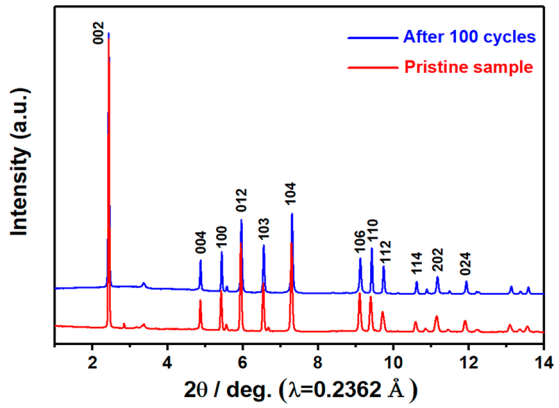

Figure 6. SXRD patterns of a $Na_{0.66}Li_{0.18}Fe_{0.12}Mn_{0.7}O_2$ cathode before and after long-term cycling.

3.4. X-ray Absorption Spectroscopy analysis. Ex situ X-ray absorption near edge structure (XANES) spectroscopy analyses were performed to investigate the charge compensation mechanisms during charge and discharge. Figure 7 presents the normalized Mn and Fe K-edge XANES spectra of the electrode collected at different charging/discharging depths, along with the corresponding reference compounds. Figure 7a shows that the edge position of Mn XANES stays largely unchanged until it is charged to 4.5 V. The slight change of spectra shape may be attributed to the different hybridization of Mn 3d orbitals with oxygen 2p orbitals.[34,39−41] This can also be attributed to the change of local coordination environment occurring at this high voltage, as evidenced by the loss of crystallinity in the *operando* SXRD, though the nature of this low crystalline structure is unclear at this moment. Upon discharge, the shape and edge position of the Mn XANES spectra overlapped well with that of the pristine sample at 3.8 V, indicating a good recovery of the structure. The spectrum shifted to a lower energy position with the electrode further discharged to 1.5 V, suggesting the reduction of Mn^{4+} likely to Mn^{3+}. Figure 7b shows the XANES spectra of Fe. It is seen that the Fe K-edge spectra slightly shifted to high energy from pristine sample to 4.5 V, suggesting the possible oxidation of Fe^{3+} to Fe^{4+} in charge. Subsequently, the spectra shift reversely to low energy during discharge, indicating the reduction to Fe^{3+}.

3.5. Solid-State NMR Analysis. As Li is the key factor for stabilizing the structure, it is critical to investigate the fate of Li during cycling. Solid-state ^{7}Li NMR was employed to monitor Li at different states of cycling as this technique can identify different local environments of Li in both crystalline and amorphous phases.[42−44] Figure 8a shows the ^{7}Li pj-MATPASS spectra of the $Na_{0.66}Li_{0.18}Fe_{0.12}Mn_{0.7}O_2$ electrode samples at different stage of cycling. Three resonances were observed at chemical shifts of 750, 1450, and 1600 ppm for the pristine sample. Based on previous ^{7}Li NMR study of Li_2MnO_3 and

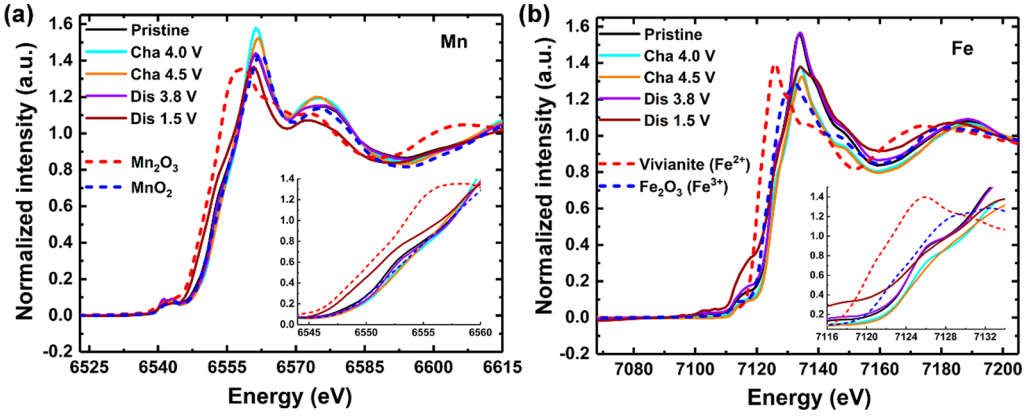

Figure 7. Ex situ XANES spectra of $Na_{0.66}Li_{0.18}Fe_{0.12}Mn_{0.7}O_2$ electrodes collected at different charge/discharge states of first cycle: (a) Mn K-edge, (b) Fe K-edge. Reference spectra of various valent states of Mn and Fe have been used to identify the valence states.

DOI: 10.1021/jacs.9b01855
J. Am. Chem. Soc. 2019, 141, 6680−6689

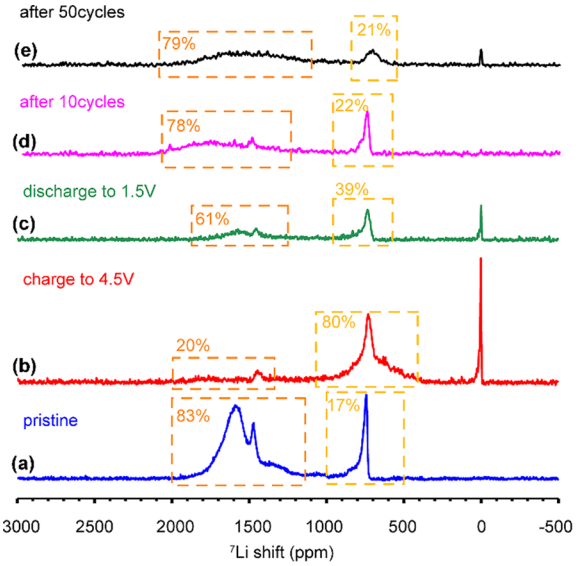

Figure 8. ^{7}Li pjMATPASS NMR spectra of $Na_{0.66}Li_{0.18}Fe_{0.12}Mn_{0.7}O_2$ electrode samples: (a) pristine powder (blue), (b) after initial charge to 4.5 V (red), (c) after first discharge to 1.5 V (olive), (d) after 10 cycles (violet), and (e) after 50 cycles (black).

other layered oxide materials,[43−45] the resonances at ∼1600 and ∼1450 ppm can be assigned to Li sites in a honeycomb-like arrangement within the transition-metal layers, while the resonance at ∼750 ppm is attributed to Li in the Na layer. These three resonances were also observed in the cycled samples. In addition, the resonance at 0 ppm observed in the cycled electrode samples can be attributed to the diamagnetic Li-containing species (such as Li_2CO_3 and LiF) likely formed on the surface of the particles due to the passivation reaction with the solvent, similar to the solid electrolyte interphase (SEI) in lithium ion batteries.

The relative amount of Li was quantified through the ^{7}Li solid-state NMR. It is worth noting that the cycled electrode was washed with PC solvent to get rid of $NaPF_6$ salt in the electrode before NMR characterization. However, the lithium-containing species on the surface of the electrode could also be washed off. Thus, we mainly focused on the total population of Li inside the lattice of the electrode. For the pristine powder, about 83% of Li resides in the transition metal layer and 17% in the sodium layer. As the formula is $Na_{0.66}Li_{0.18}Fe_{0.12}Mn_{0.7}O_2$, according to this NMR quantification, the crystallographic site occupancy of Li in sodium layer is 17% × 0.18 = 0.03, which agrees with the design motivation that Li prefers to occupy the octahedral sites in the TM layers and further confirms that the major part of Li is indeed doped into the TM layer. After being charged to 4.5 V, Li in TM layer decreased to 20% and Li in sodium layer increased to 80%, indicating most Li in the TM layer migrated to the sodium layers. As indicated by in situ XRD results, at this stage the structure of the electrode is still P2, despite the increased disordering as suggested by the lower and broader Bragg peaks. The diffusion of Li^+ through the large prismatic site is expected to be much more impeded than that of Na^+, which is speculated to result in the accumulation of Li in Na sites rather than removal of Li out of the lattice. When discharged back to 1.5 V, Li in TM layers increased to 61%, while Li in sodium layer decreased to 39%, indicating the migration of Li between TM and Na layers is partially reversible. This is because Li prefers to stay in the octahedral sites in the TM layer rather than in the prismatic sites in Na layer. In the samples that are cycled for 10 and 50 cycles, it is quite exciting to see that the Li distribution between the two environments seems to reach an equilibrium, with Li in Na layer being ∼20% and Li in TM layer being ∼80% at the fully discharged state. Despite that the total amount of Li in the lattice is lower in samples after extensive cycles than in pristine samples, the concentration of remaining Li in the TM layer seems to be still sufficient to maintain the structure in P2 and to eliminate the P2−O2 transition.

4. DISCUSSION

To better understand the synergistic effect of Li and Fe codoping on the cycling stability of $Na_{0.66}Li_{0.18}Fe_{0.12}Mn_{0.7}O_2$, its performance was compared with that of Li-free and Fe-free cathode materials. As shown in Table S1, the reversible capacity and the capacity retention of $Na_{0.66}Li_{0.18}Fe_{0.12}Mn_{0.7}O_2$ were superior to those of most previously reported materials. This is mainly due to the fact that it shows a solid solution pathway in cycling and the P2−O2 transition is completely eliminated in a fairly wide voltage window of 1.5−4.5 V, while the cycling of most Li-free materials was limited to cycling below 4.1 V to maintain reasonable capacity retention. In comparison with the Li-doped materials, such as P2−$Na_{0.6}Li_{0.2}Mn_{0.8}O_2$, the performance of $Na_{0.66}Li_{0.18}Fe_{0.12}Mn_{0.7}O_2$ is also superior. Figure 9a shows the cycling performance of

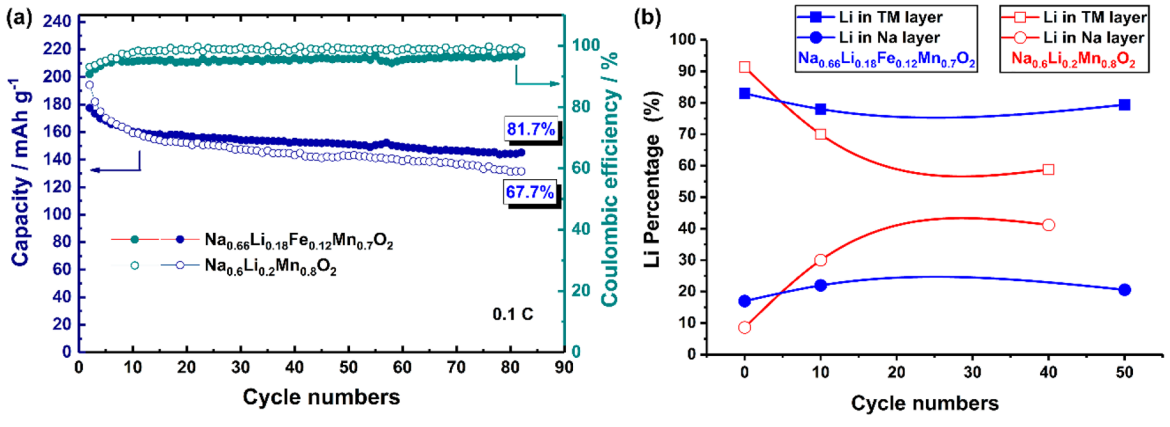

Figure 9. (a) Cycling performance of $Na_{0.6}Li_{0.2}Mn_{0.8}O_2$ and $Na_{0.66}Li_{0.18}Fe_{0.12}Mn_{0.7}O_2$ cathodes in a half cell within 1.5−4.5 V. (b) Variation of fractions of Li in TM layers and Li in Na layers for $Na_{0.6}Li_{0.2}Mn_{0.8}O_2$ and $Na_{0.66}Li_{0.18}Fe_{0.12}Mn_{0.7}O_2$.

DOI: 10.1021/jacs.9b01855
J. Am. Chem. Soc. 2019, 141, 6680−6689

$Na_{0.6}Li_{0.2}Mn_{0.8}O_2$ and $Na_{0.66}Li_{0.18}Fe_{0.12}Mn_{0.7}O_2$. Both cathodes were cycled in a wide voltage range from 1.5−4.5 V at the same rate of 0.1 C in half-cells assembled in standard coin cells. Though the Fe-free $Na_{0.6}Li_{0.2}Mn_{0.8}O_2$ cathode exhibits a higher initial capacity than that of $Na_{0.66}Li_{0.18}Fe_{0.12}Mn_{0.7}O_2$, $Na_{0.66}Li_{0.18}Fe_{0.12}Mn_{0.7}O_2$ exhibits a much better capacity retention with higher remaining capacity than that of the Fe-free cathode after 82 cycles (81.7% vs 67.7%). This indicates the beneficial effect of Fe-doping for the enhanced cyclability of $Na_{0.66}Li_{0.18}Fe_{0.12}Mn_{0.7}O_2$. Since Li in the TM is the key feature to stabilize the P2 structure, the fate of Li in cycling in both materials needs to be carefully tracked and compared.

We normalized the total amount of Li in the TM layer and sodium layer to be 100% based on the NMR results of both electrode materials after different number of cycles (the quantitative NMR results of $Na_{0.6}Li_{0.2}Mn_{0.8}O_2$ can be found in more details in our previous publication[12]). As shown in Figure 9b with the red dots and line, it can be seen that the Li distribution in $Na_{0.6}Li_{0.2}Mn_{0.8}O_2$ cathode experienced a major change upon extended cycling. The fraction of Li in the TM layer progressively drops from 91.4% to 58.8% in 40 cycles. Meanwhile, the fraction of Li in the sodium layer progressively increases from 8.6% to 41.2%, while the fractions of Li in the TM layer in $Na_{0.66}Li_{0.18}Fe_{0.12}Mn_{0.7}O_2$ electrode (shown in blue dots and line) only slightly drop upon cycling, from 83% in pristine to 79.4% after 50 cycles. This result indicates that the Fe dopant in the TM layer can better mitigate the Li loss from TM layer than Mn, which we believe to be a critical factor to allow the excellent capacity retention. Unfortunately, further increasing the amount of Fe in the starting materials results in more O3 structured secondary phase (Figure S1) and does not further improve the capacity and retention. It is not necessary for Fe to be the best dopant to help keep Li in the lattice, and the composition of $Na_{0.66}Li_{0.18}Fe_{0.12}Mn_{0.7}O_2$ is not necessarily optimal, but the encouraging improvement in capacity and retention in $Na_{0.66}Li_{0.18}Fe_{0.12}Mn_{0.7}O_2$ warrants the necessity for further investigation on the correlation between Li in the Na layer and the transition metals in the TM layer in order to better keep Li in the lattice and further improve the cycling capacity and stability.

The initial charge capacity (343 mAh g^{-1}) exceeds the theoretical capacity (234 mAh g^{-1}), calculated solely based on the redox of transition metals (Fe and Mn), which implies that a part of the capacity may be involved with either the side reaction with the electrolyte or the oxidation of oxygen, possibly including irreversible O2 release and some portion of reversible redox of lattice oxygen.[46,47] The redox of lattice oxygen is triggered by the special bonding environment of oxygen with alkaline metal ions in both the TM layer and alkaline metal layer, similar to what has been frequently observed and extensively discussed in the Li- and Mn-rich layered cathode in lithium ion batteries.[30,33,34] Therefore, for this reason, it is also critical to keep sufficient amount lithium in the lattice to keep the oxygen related redox active during cycling.[48] Compared with $Na_{0.6}Li_{0.2}Mn_{0.8}O_2$, $Na_{0.66}Li_{0.18}Fe_{0.12}Mn_{0.7}O_2$ is able to keep more Li in the lattice for a longer cycling time. This may be related to the stability of the vacancies in the TM layer left by the Li ions hopping into the Na layer, but at this point, it was not clear what configuration or combination of cation in the TM layer would have the best lithium keeping effect. In addition, the combination of Fe and Mn is speculated to have significant impact on the manner of oxygen evolution. There remaining questions warrant research to further exploring these group of Li doped P2 cathode materials in more aspects.

5. CONCLUSION

In this work, a novel cathode material for sodium ion batteries, namely $Na_{0.66}Li_{0.18}Fe_{0.12}Mn_{0.7}O_2$, was designed based on the strategy of using lithium to stabilize the deeply charge structure and was successfully synthesized. The high discharge capacity of ~210 mA g^{-1} and the excellent cycle stability shows the high promise of this materials. Analysis based on in situ and ex situ structure characterizations revealed that multiple factors are key to achieve this high performance: (1) the irreversible P2−O2 phase transition is eliminated within a wide voltage range of 1.5−4.5 V, so to achieve a highly reversible phase evolution pathway and small volume change; (2) lithium is effectively kept in the lattice and can partly reversibly hop between the transition metal layer and alkaline metal layer. The high performance of $Na_{0.66}Li_{0.18}Fe_{0.12}Mn_{0.7}O_2$ demonstrated the effectiveness of Li and Fe co-doping and opens up opportunities to design more structure stabilized layered oxide cathodes and achieve high capacity and long cycle life.

■ ASSOCIATED CONTENT

Supporting Information

The Supporting Information is available free of charge on the ACS Publications website at DOI: 10.1021/jacs.9b01855.

XRD patterns of $Na_xLi_yFe_zMn_{(1-y-z)}O_2$, charge/discharge profiles; comparison of electrochemical performance with previous reports, *operando* lab X-ray diffraction patterns, fitted lab X-ray diffraction patterns, and the evolution of lattice parameters upon cycling (PDF)

■ AUTHOR INFORMATION

Corresponding Author

*hailong.chen@me.gatech.edu

ORCID

Jue Liu: 0000-0002-4453-910X
Yuanzhi Tang: 0000-0002-7741-8646
Yan-Yan Hu: 0000-0003-0677-5897
Meilin Liu: 0000-0002-6188-2372
Hailong Chen: 0000-0001-8283-2860

Notes

The authors declare no competing financial interest.

■ ACKNOWLEDGMENTS

This work was supported by the U.S. National Science Foundation under Grant Nos. DMR-1410936, DMR-1706723, and DMR-1210792. The authors acknowledge Dr. Eric Dooryhee for help with synchrotron data collection. H.C., X.M, S.X., and L.Y. acknowledge financial support from the Georgia Tech new faculty startup fund. Y.-Y.H. and X.L. acknowledge support from the National Science Foundation under Grant No. DMR-1508404. All NMR experiments were carried out at the NHMFL supported by NSF under Contract No. DMR-1157490. This research used the XPD (28-ID-2) beamline of the National Synchrotron Light Sourch II, a U.S. Department of Energy (DOE) Office of Science User Facility operated for the DOE Office of Science by Brookhaven National Laboratory under Contract No. DE-SC0012704. This research used Beamline 17-BM of the Advanced Photon Source, a U.S. DOE Office of Science User Facility operated

DOI: 10.1021/jacs.9b01855
J. Am. Chem. Soc. 2019, 141, 6680−6689

for the DOE Office of Science by Argoone National Laboratory under Contract No. DE-AC02-06CH11357. Research conducted at the NOMAD beamline at ORNL's Spallation Neutron Source was sponsored by the Scientific User Facilities Division, Office of Basic Sciences, U.S. Department of Energy.

REFERENCES

(1) Wang, P. F.; You, Y.; Yin, Y. X.; Guo, Y. G. Layered Oxide Cathodes for Sodium−Ion Batteries: Phase Transition, Air Stability, and Performance. *Adv. Energy Mater.* **2018**, *8* (8), 1701912.

(2) Kubota, K.; Kumakura, S.; Yoda, Y.; Kuroki, K.; Komaba, S. Electrochemistry and Solid−State Chemistry of $NaMeO_2$ (Me= 3d Transition Metals). *Adv. Energy Mater.* **2018**, *8* (17), 1703415.

(3) Delmas, C.; Fouassier, C.; Hagenmuller, P. Structural classification and properties of the layered oxides. *Physica B+C* **1980**, *99* (1−4), 81−85.

(4) Xu, G. L.; Amine, R.; Abouimrane, A.; Che, H.; Dahbi, M.; Ma, Z. F.; Saadoune, I.; Alami, J.; Mattis, W. L.; Pan, F. Challenges in Developing Electrodes, Electrolytes, and Diagnostics Tools to Understand and Advance Sodium−Ion Batteries. *Adv. Energy Mater.* **2018**, *8* (14), 1702403.

(5) Lu, Z.; Dahn, J. In Situ X-Ray Diffraction Study of P2 $Na_{2/3}[Ni_{1/3}Mn_{2/3}]O_2$. *J. Electrochem. Soc.* **2001**, *148* (11), A1225−A1229.

(6) Radin, M. D.; Van der Ven, A. Simulating Charge, Spin, and Orbital Ordering: Application to Jahn−Teller Distortions in Layered Transition-Metal Oxides. *Chem. Mater.* **2018**, *30* (3), 607−618.

(7) Radin, M. D.; Alvarado, J.; Meng, Y. S.; Van der Ven, A. Role of Crystal Symmetry in the Reversibility of Stacking-Sequence Changes in Layered Intercalation Electrodes. *Nano Lett.* **2017**, *17* (12), 7789−7795.

(8) Dose, W. M.; Sharma, N.; Pramudita, J. C.; Kimpton, J. A.; Gonzalo, E.; Han, M. H.; Rojo, T. Crystallographic evolution of P2 $Na_{2/3}Fe_{0.4}Mn_{0.6}O_2$ electrodes during electrochemical cycling. *Chem. Mater.* **2016**, *28* (17), 6342−6354.

(9) Thorne, J.; Dunlap, R.; Obrovac, M. Structure and electrochemistry of $Na_xFe_yMn_{1-y}O_2$ ($1.0 \leq y \leq 0.5$) for Na-ion battery positive electrodes. *J. Electrochem. Soc.* **2013**, *160* (2), A361−A367.

(10) Mortemard de Boisse, B.; Carlier, D.; Guignard, M.; Bourgeois, L.; Delmas, C. P2-$Na_xMn_{1/2}Fe_{1/2}O_2$ phase used as positive electrode in Na batteries: structural changes induced by the electrochemical (de) intercalation process. *Inorg. Chem.* **2014**, *53* (20), 11197−11205.

(11) Wang, P. F.; You, Y.; Yin, Y. X.; Wang, Y. S.; Wan, L. J.; Gu, L.; Guo, Y. G. Suppressing the P2−O2 Phase Transition of $Na_{0.67}Mn_{0.67}Ni_{0.33}O_2$ by Magnesium Substitution for Improved Sodium−Ion Batteries. *Angew. Chem., Int. Ed.* **2016**, *55* (26), 7445−7449.

(12) Yang, L.; Li, X.; Ma, X.; Xiong, S.; Liu, P.; Tang, Y.; Cheng, S.; Hu, Y.-Y.; Liu, M.; Chen, H. Design of high-performance cathode materials with single-phase pathway for sodium ion batteries: A study on P2-$Na_x(Li_yMn_{1-y})O_2$ compounds. *J. Power Sources* **2018**, *381*, 171−180.

(13) Han, M. H.; Gonzalo, E.; Sharma, N.; Lçpez del Amo, J. M.; Armand, M.; Avdeev, M.; Saiz Garitaonandia, J. J.; Rojo, T. f. High-performance P2-phase $Na_{2/3}Mn_{0.8}Fe_{0.1}Ti_{0.1}O_2$ cathode material for ambient-temperature sodium-ion batteries. *Chem. Mater.* **2016**, *28* (1), 106−116.

(14) Kim, D.; Kang, S. H.; Slater, M.; Rood, S.; Vaughey, J. T.; Karan, N.; Balasubramanian, M.; Johnson, C. S. Enabling sodium batteries using lithium−substituted sodium layered transition metal oxide cathodes. *Adv. Energy Mater.* **2011**, *1* (3), 333−336.

(15) Xu, J.; Lee, D. H.; Clément, R. J.; Yu, X.; Leskes, M.; Pell, A. J.; Pintacuda, G.; Yang, X.-Q.; Grey, C. P.; Meng, Y. S. Identifying the critical role of Li substitution in P2−$Na_x[Li_yNi_zMn_{1-y-z}]O_2$ (0< x, y, z< 1) intercalation cathode materials for high-energy Na-ion batteries. *Chem. Mater.* **2014**, *26* (2), 1260−1269.

(16) Clément, R. J.; Billaud, J.; Armstrong, A. R.; Singh, G.; Rojo, T.; Bruce, P. G.; Grey, C. P. Structurally stable Mg-doped P2-$Na_{2/3}Mn_{1-}Mg_yO_2$ sodium-ion battery cathodes with high rate performance: insights from electrochemical, NMR and diffraction studies. *Energy Environ. Sci.* **2016**, *9* (10), 3240−3251.

(17) Mu, L.; Hou, Q.; Yang, Z.; Zhang, Y.; Rahman, M. M.; Kautz, D. J.; Sun, E.; Du, X.-W.; Du, Y.; Nordlund, D. Water-Processable P2-$Na_{0.67}Ni_{0.22}Cu_{0.11}Mn_{0.56}Ti_{0.11}O_2$ Cathode Material for Sodium Ion Batteries. *J. Electrochem. Soc.* **2019**, *166* (2), A251−A257.

(18) Rahman, M. M.; Xu, Y.; Cheng, H.; Shi, Q.; Kou, R.; Mu, L.; Liu, Q.; Xia, S.; Xiao, X.; Sun, C.-J. Empowering multicomponent cathode materials for sodium ion batteries by exploring three-dimensional compositional heterogeneities. *Energy Environ. Sci.* **2018**, *11* (9), 2496−2508.

(19) Clément, R. J.; Bruce, P. G.; Grey, C. P. manganese-based P2-type transition metal oxides as sodium-ion battery cathode materials. *J. Electrochem. Soc.* **2015**, *162* (14), A2589−A2604.

(20) Clément, R.; Xu, J.; Middlemiss, D.; Alvarado, J.; Ma, C.; Meng, Y.; Grey, C. Direct evidence for high Na+ mobility and high voltage structural processes in P2-$Na_x[Li_y\ Ni_zMn_z]O2$ (x, y, z≤ 1) cathodes from solid-state NMR and DFT calculations. *J. Mater. Chem. A* **2017**, *5* (8), 4129−4143.

(21) Bianchini, M.; Gonzalo, E.; Drewett, N. E.; Ortiz-Vitoriano, N.; López del Amo, J. M. L.; Bonilla, F. J.; Acebedo, B.; Rojo, T. Layered P2−O3 sodium-ion cathodes derived from earth abundant elements. *J. Mater. Chem. A* **2018**, *6* (8), 3552−3559.

(22) Ma, X.; An, K.; Bai, J.; Chen, H. $NaAlTi_3O_8$, A Novel Anode Material for Sodium Ion Battery. *Sci. Rep.* **2017**, *7* (1), 162.

(23) Chen, H.; Hao, Q.; Zivkovic, O.; Hautier, G.; Du, L.-S.; Tang, Y.; Hu, Y.-Y.; Ma, X.; Grey, C. P.; Ceder, G. Sidorenkite ($Na_3MnPO_4CO_3$): a new intercalation cathode material for Na-ion batteries. *Chem. Mater.* **2013**, *25* (14), 2777−2786.

(24) Wang, Y.; Pan, Z.; Ho, Y.; Xu, Y.; Du, A. Nuclear instruments and methods in physics research section B: beam interactions with materials and atoms. *Nucl. Instrum. Methods Phys. Res., Sect. B* **2001**, *180* (1−4), 251−256.

(25) Cheary, R. W.; Coelho, A. A.; Cline, J. P. Fundamental parameters line profile fitting in laboratory diffractometers. *J. Res. Natl. Inst. Stand. Technol.* **2004**, *109* (1), 1.

(26) Yabuuchi, N.; Hara, R.; Kajiyama, M.; Kubota, K.; Ishigaki, T.; Hoshikawa, A.; Komaba, S. New O2/P2 type Li Excess Layered Manganese Oxides as Promising Multi−Functional Electrode Materials for Rechargeable Li/Na Batteries. *Adv. Energy Mater.* **2014**, *4* (13), 1301453.

(27) Yabuuchi, N.; Yoshii, K.; Myung, S.-T.; Nakai, I.; Komaba, S. Detailed studies of a high-capacity electrode material for rechargeable batteries, Li_2MnO_3 $LiCo_{1/3}Ni_{1/3}Mn_{1/3}O_2$. *J. Am. Chem. Soc.* **2011**, *133* (12), 4404−4419.

(28) Assat, G.; Tarascon, J.-M. Fundamental understanding and practical challenges of anionic redox activity in Li-ion batteries. *Nature Energy* **2018**, *3*, 373.

(29) Maitra, U.; House, R. A.; Somerville, J. W.; Tapia-Ruiz, N.; Lozano, J. G.; Guerrini, N.; Hao, R.; Luo, K.; Jin, L.; Pérez-Osorio, M. A. Oxygen redox chemistry without excess alkali-metal ions in $Na_{2/3}[Mg_{0.28}Mn_{0.72}]O_2$. *Nat. Chem.* **2018**, *10* (3), 288.

(30) Seo, D.-H.; Lee, J.; Urban, A.; Malik, R.; Kang, S.; Ceder, G. The structural and chemical origin of the oxygen redox activity in layered and cation-disordered Li-excess cathode materials. *Nat. Chem.* **2016**, *8* (7), 692.

(31) Wang, J.; He, X.; Paillard, E.; Laszczynski, N.; Li, J.; Passerini, S. Lithium−and Manganese-Rich Oxide Cathode Materials for High-Energy Lithium Ion Batteries. *Adv. Energy Mater.* **2016**, *6* (21), 1600906.

(32) Koga, H.; Croguennec, L.; Ménétrier, M.; Mannessiez, P.; Weill, F.; Delmas, C.; Belin, S. Operando X-ray absorption study of the redox processes involved upon cycling of the Li-rich layered oxide $Li_{1.20}Mn_{0.54}Co_{0.13}Ni_{0.13}O_2$ in Li ion batteries. *J. Phys. Chem. C* **2014**, *118* (11), 5700−5709.

DOI: 10.1021/jacs.9b01855
J. Am. Chem. Soc. 2019, 141, 6680−6689

(33) Sathiya, M.; Rousse, G.; Ramesha, K.; Laisa, C.; Vezin, H.; Sougrati, M. T.; Doublet, M.-L.; Foix, D.; Gonbeau, D.; Walker, W. Reversible anionic redox chemistry in high-capacity layered-oxide electrodes. *Nat. Mater.* **2013**, *12* (9), 827.
(34) Luo, K.; Roberts, M. R.; Hao, R.; Guerrini, N.; Pickup, D. M.; Liu, Y.-S.; Edström, K.; Guo, J.; Chadwick, A. V.; Duda, L. C. Charge-compensation in 3d-transition-metal-oxide intercalation cathodes through the generation of localized electron holes on oxygen. *Nat. Chem.* **2016**, *8* (7), 684.
(35) Hasa, I.; Buchholz, D.; Passerini, S.; Hassoun, J. A comparative study of layered transition metal oxide cathodes for application in sodium-ion battery. *ACS Appl. Mater. Interfaces* **2015**, *7* (9), 5206−5212.
(36) Yuan, D.; Hu, X.; Qian, J.; Pei, F.; Wu, F.; Mao, R.; Ai, X.; Yang, H.; Cao, Y. P2-type $Na_{0.67}Mn_{0.65}Fe_{0.2}Ni_{0.15}O_2$ cathode material with high-capacity for sodium-ion battery. *Electrochim. Acta* **2014**, *116*, 300−305.
(37) Yabuuchi, N.; Kajiyama, M.; Iwatate, J.; Nishikawa, H.; Hitomi, S.; Okuyama, R.; Usui, R.; Yamada, Y.; Komaba, S. P2-type $Na_x[Fe_{1/2}Mn_{1/2}]O_2$ made from earth-abundant elements for rechargeable Na batteries. *Nat. Mater.* **2012**, *11* (6), 512.
(38) Ma, X.; Chen, H.; Ceder, G. Electrochemical properties of monoclinic $NaMnO_2$. *J. Electrochem. Soc.* **2011**, *158* (12), A1307−A1312.
(39) Xu, J.; Sun, M.; Qiao, R.; Renfrew, S. E.; Ma, L.; Wu, T.; Hwang, S.; Nordlund, D.; Su, D.; Amine, K. Elucidating anionic oxygen activity in lithium-rich layered oxides. *Nat. Commun.* **2018**, *9* (1), 947.
(40) Qiao, Y.; Guo, S.; Zhu, K.; Liu, P.; Li, X.; Jiang, K.; Sun, C.-J.; Chen, M.; Zhou, H. Reversible anionic redox activity in Na_3RuO_4 cathodes: a prototype Na-rich layered oxide. *Energy Environ. Sci.* **2018**, *11* (2), 299−305.
(41) Gent, W. E.; Lim, K.; Liang, Y.; Li, Q.; Barnes, T.; Ahn, S.-J.; Stone, K. H.; McIntire, M.; Hong, J.; Song, J. H. Coupling between oxygen redox and cation migration explains unusual electrochemistry in lithium-rich layered oxides. *Nat. Commun.* **2017**, *8* (1), 2091.
(42) Li, X.; Tang, M.; Feng, X.; Hung, I.; Rose, A.; Chien, P.-H.; Gan, Z.; Hu, Y.-Y. Lithiation and Delithiation Dynamics of Different Li Sites in Li-Rich Battery Cathodes Studied by Operando Nuclear Magnetic Resonance. *Chem. Mater.* **2017**, *29* (19), 8282−8291.
(43) Lee, Y. J.; Wang, F.; Grey, C. P. 6Li and 7Li MAS NMR studies of lithium manganate cathode materials. *J. Am. Chem. Soc.* **1998**, *120* (48), 12601−12613.
(44) Grey, C. P.; Dupré, N. NMR studies of cathode materials for lithium-ion rechargeable batteries. *Chem. Rev.* **2004**, *104* (10), 4493−4512.
(45) Bowden, W.; Bofinger, T.; Zhang, F.; Iltchev, N.; Sirotina, R.; Paik, Y.; Chen, H.; Grey, C.; Hackney, S. New manganese dioxides for lithium batteries. *J. Power Sources* **2007**, *165* (2), 609−615.
(46) Dai, K.; Wu, J.; Zhuo, Z.; Li, Q.; Sallis, S.; Mao, J.; Ai, G.; Sun, C.; Li, Z.; Gent, W. E. High Reversibility of Lattice Oxygen Redox Quantified by Direct Bulk Probes of Both Anionic and Cationic Redox Reactions. *Joule* **2019**, *3* (2), 518−541.
(47) Yang, W.; Devereaux, T. P. Anionic and cationic redox and interfaces in batteries: Advances from soft X-ray absorption spectroscopy to resonant inelastic scattering. *J. Power Sources* **2018**, *389*, 188−197.
(48) Ben Yahia, M.; Vergnet, J.; Saubanère, M.; Doublet, M.-L. Unified picture of anionic redox in Li/Na-ion batteries. *Nat. Mater.* **2019**, 1.

DOI: 10.1021/jacs.9b01855
J. Am. Chem. Soc. 2019, 141, 6680−6689